

## Phase Diagram of Rod–Coil Diblock Copolymer Melts

Jiuzhou Tang,<sup>†</sup> Ying Jiang,<sup>‡</sup> Xinghua Zhang,<sup>§</sup> Dadong Yan,<sup>\*,||</sup> and Jeff Z. Y. Chen<sup>\*,†</sup>

<sup>†</sup>Beijing National Laboratory For Molecular Sciences (BNLMS), Laboratory of Polymer Physics and Chemistry, Institute of Chemistry, Chinese Academy of Sciences, Beijing 100190, China

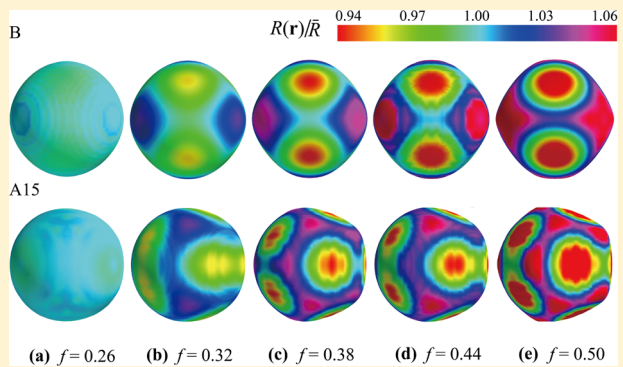
<sup>‡</sup>School of Chemistry and Environment, Beihang University, Beijing 100083, China

<sup>§</sup>School of Science, Beijing Jiaotong University, Beijing 100044, China

<sup>||</sup>Department of Physics, Beijing Normal University, Beijing 100875, China

<sup>†</sup>Department of Physics and Astronomy, University of Waterloo, Waterloo, Ontario, Canada N2L 3G1

**ABSTRACT:** A unified phase diagram is presented for rod–coil diblock copolymer melts in the isotropic phase regime as a function of the asymmetric parameter. The study is based on free energy calculation, which incorporates three-dimensional spatial variations of the volume fraction with angular dependence. The wormlike-chain model is used in a self-consistent field treatment. Body-centered cubic, A15, hexagonal, gyroid, and lamellar structures where the rod segments are packed inside the convex rod–coil interface are found stable. As the conformational asymmetric parameter increases, the A15 phase region expands and the gyroid phase region reduces. The stability of the structures is analyzed by concepts such as packing frustration, spinodal limit, and interfacial curvature.



### 1. INTRODUCTION

Self-assembly of block copolymers has drawn great attention in recent years due to the promise of forming a rich variety of nanostructures potentially useful in applications.<sup>1</sup> Block copolymers consisting of rigid and flexible blocks are commonly known as rod–coil block copolymers. The rigid block of rod–coil copolymers can have interesting electrical and photoactive properties that can be exploited in device making. For example, the practical application of organic optoelectronic devices requires the self-assembly of such copolymers.<sup>2–4</sup> In general, the rod block can be made from conjugated backbone, aromatic groups, or even the helical secondary structure of a peptide.<sup>5</sup>

Experimental studies on self-assembly of rod–coil copolymers have suggested remarkably rich structural morphologies arising from the microphase separation driven by immiscibility and orientation-dependent interaction. So far, morphologies such as smectic A, smectic C, lamellar, hexagonally perforated lamellar, hexagonal cylinder, gyroid, body-centered cubic, and zigzag structures have been observed in variety of rod–coil diblock copolymer melts.<sup>6–12</sup> This has provided a wide playground for manipulating microstructure by alternating molecular level architectures.

Past decades have witnessed surging interests on theoretical understanding of flexible–flexible block copolymers, particularly due to success of the self-consistent field theory (SCFT) that incorporates the Gaussian-chain (GSC) model for description of both flexible polymer blocks.<sup>13–15</sup> The SCFT formalism can also be developed for rod–coil copolymers

following the same idea, treating the flexible block as GSC.<sup>16–18</sup> The rigid block is usually modeled by a rod, which typically has an orientation. The rigid segment behaves quite differently from the flexible block because of its lacking of the conformational entropy; in replacement, the orientational entropy becomes more important. Depending on the physical system, the rod–rod interaction arising from different polymer chains can also produce orientationally dependent interactions, typically seen in a liquid-crystal system. The self-assembly of rod–coil block copolymers forms a distinct class of problems in polymer physics.

Theoretical studies on self-assembly of rod–coil copolymers are far from complete because of a couple of reasons. First, the typical formalism involves spatial inhomogeneity coupled with orientational ordering of polymer segments. The coupling requires the specification of both spatial variables and orientational variables mathematically, hence creating the computational challenge to handle multidimensional variables; this can be contrasted with a typical SCFT for flexible–flexible block copolymer melts which normally involves the spatial variation only. The SCFT formalism for semiflexible–semi-flexible diblock copolymer melts is generally possible by incorporating the wormlike-chain (WLC) model, as outlined in section 2.1. With the appropriate identification of the persistence lengths, the formalism can be used to study rod–

Received: October 9, 2015

Revised: November 22, 2015

Published: December 10, 2015

coil systems. As has been highlighted in recent publications, an algorithm that exploits a simple parallel computational environment is now possible to tackle a problem that depends on both positional and orientational variables.<sup>19,20</sup> This enables the current work numerically.

In addition, as discussed in section 2.2, there are a number of physical parameters in the system that yields a multidimensional parameter space. The interaction between diblock copolymers is commonly modeled by the Flory–Huggins interaction parameter  $\chi$ , which shows up in a typical theory as a combination  $\chi N$  where  $N$  is the degree of polymerization along the entire chain. The volume fraction of one of the components, for example the rod blocks, gives rise to the second parameter  $f$ . In a conformationally symmetric flexible–flexible block copolymer problem these are the two essential parameters. Here, for the rod–coil problem, a third parameter that measures the inherited conformational asymmetries in the two blocks,  $\nu$ , is needed.<sup>17</sup> To complicate the matter further, in a theory that includes the orientational interaction, an additional parameter, for example the Maier–Saupe coefficient  $\mu$ , needs to be considered.<sup>21</sup> Investigating the complete phase behavior in the entire  $\chi N$ – $f$ – $\nu$ – $\mu$  space is a daunting task, and previous efforts usually focus on a specific area of this four-dimensional parameter space.<sup>17,22–27</sup>

Even for the physically meaningful subspace,  $\chi N$ – $f$ – $\nu$ , a comprehensive theoretical understanding for different  $\nu$  is not available. This is a case where  $\mu = 0$  and the polymers are in the isotropic phases (in the liquid-crystal language), similar to those in the coil–coil block copolymer problem. Using SCFT, Müller and Schick examined the case  $\nu^{-2} = 50$ ,<sup>16</sup> and Reenders and ten Brinke examined the case  $\nu^{-2} = 40$ .<sup>24</sup> Using the lattice simulation techniques, both Li and Gersappe as well as Chen et al. examined the case  $\nu^{-2} = 20$ .<sup>26,28</sup> When all these phase diagrams are placed together for comparison, as discussed in section 3.2, major differences can be found.

In this paper, we aim at investigating the  $\chi N$ – $f$ – $\nu$  phase space thoroughly using the SCFT procedure recently developed for wormlike block copolymers. The results are displayed in terms of the traditional  $\chi N$ – $f$  phase diagrams for various  $\nu$  (sections 3.1 and 3.2). Classical structures found from diblock copolymer self-assembly are observed, together with the much anticipated A15 structure which is found in high conformational asymmetric cases (see Figure 1). The emergence of the gyroid phase is confirmed only in small- $\nu^{-2}$  systems. The

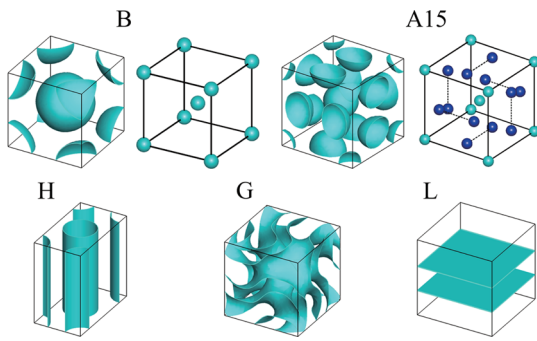


**Figure 1.** Structures found in this work. These plots represent the interfaces between A- and B-rich domains of body-centered cubic spheres (B), A15 spheres (A15), hexagonal cylinders (H), gyroid (G), and lamellar (L) phases. For clarification, in separate plots, spheres at the cubic corners and centers are colored in green, and spheres near the face centers are colored in blue for both B and A15.

lacking of the coil-centered structures is addressed in section 3.3. The structural properties of the ordered states are analyzed in light of concepts such as interfacial curvature and packing frustration in section 3.4. The order-to-disorder transition curves are discussed in association with the interfacial width in section 3.5. Finally, the orientation distributions of the rod blocks are shown by orientation maps in section 3.6.

## 2. THEORY

**2.1. Basic Formalism.** In this section, we outline the self-consistent-field theory for the current system, developed on the basis of the continuum version of the WLC model. The system is composed of  $n$  monodisperse semiflexible–semiflexible diblock copolymer chains in volume  $V$ . Later we will specify the persistence lengths  $\lambda_C$  and  $\lambda_R$  for the coil and rod blocks.

The monomeric units are assumed to have the statistical segment lengths  $a_C$  and  $a_R$  for the coil block and the rod block, respectively. A single rod–coil chain contains a total of  $N$  such segments,  $fN$  in the rod block, and  $(1-f)N$  in the coil block. The total contour length for the entire chain is then  $L \equiv fNa_R + (1-f)Na_C$ . The volume occupied by a segment, either  $a_R$  or  $a_C$ , is assumed to have a common magnitude  $\rho_0^{-1} = V/(Nn)$ .

The configuration of the  $k$ th polymer chain is described by a space curve represented by the spatial coordinate  $\mathbf{R}_k(s)$ , in which  $s$  is an arc variable along the curve, continuously varying from the rod-block terminal ( $s = 0$ ) to the flexible-block terminal ( $s = L$ ). The unit tangent vector  $\mathbf{u}_k(s) \equiv d\mathbf{R}_k(s)/ds$  specifies the local orientation at location  $s$  of the  $k$ th polymer chain. We can then write the total bending energy  $H_0$  of the wormlike chains in the entire system<sup>29</sup>

$$\beta H_0 = \frac{\lambda_R}{2} \sum_{k=1}^n \int_0^{fNa_R} ds \left| \frac{d\mathbf{u}_k(s)}{ds} \right|^2 + \frac{\lambda_C}{2} \sum_{k=1}^n \int_{fNa_R}^L ds \left| \frac{d\mathbf{u}_k(s)}{ds} \right|^2 \quad (1)$$

where  $\beta = 1/k_B T$  with  $k_B$  the Boltzmann constant and  $T$  the temperature.

Next we introduce a reduced variable  $t$  such that

$$dt = ds \times \begin{cases} (Na_R)^{-1}, & \text{if } 0 \leq s \leq f \\ (Na_C)^{-1}, & \text{if } f < s \leq 1 \end{cases}$$

which is a variable that measures the fraction of statistical segments along a chain. We can then write the configuration-dependent volume fractions of the two components as

$$\hat{\phi}_R(\mathbf{r}) \equiv \frac{N}{\rho_0} \sum_{k=1}^n \int_0^f dt \delta(\mathbf{r} - \mathbf{R}_k(t)) \quad (2)$$

$$\hat{\phi}_C(\mathbf{r}) \equiv \frac{N}{\rho_0} \sum_{k=1}^n \int_f^1 dt \delta(\mathbf{r} - \mathbf{R}_k(t)) \quad (3)$$

With this notation, the local immiscibility interaction can be described by the energy penalty of mixing the two types of segments, in the typical Flory–Huggins form<sup>30</sup>

$$\beta H_I = \chi \rho_0 \int d\mathbf{r} \hat{\phi}_C(\mathbf{r}) \hat{\phi}_R(\mathbf{r}) \quad (4)$$

where  $\chi$  is the Flory–Huggins coefficient. The immiscibility interaction between the two components alone drives the microphase separation of the melt consisting of rod–coil diblock copolymers. The same mechanism causes phase separation in flexible–flexible and semiflexible–semiflexible

block copolymer melts.<sup>16,19,23,26,31,32</sup> No other interaction is assumed here, although for liquid-crystal phases, one can add, for example, a Maier–Saupe interaction energy into the formalism.<sup>21,33</sup> Without such a term, the current model deals with the isotropic interaction between polymer segments, at the same level as other rod–coil models considered under similar conditions.<sup>16,26,28</sup>

Taking the Hubbard–Stratonovich transformation and the saddle-point approximation<sup>34</sup> leads to the mean-field Helmholtz free energy per chain

$$\beta F = -\ln Q + \frac{1}{V} \int d\mathbf{r} \{ \chi N \phi_C(\mathbf{r}) \phi_R(\mathbf{r}) - w_C(\mathbf{r}) \phi_C(\mathbf{r}) \\ - w_R(\mathbf{r}) \phi_R(\mathbf{r}) + \xi(\mathbf{r}) [\phi_C(\mathbf{r}) + \phi_R(\mathbf{r}) - 1] \} \quad (5)$$

In this expression,  $\phi_C(\mathbf{r})$  and  $\phi_R(\mathbf{r})$  are the mean volume fractions,  $w_C(\mathbf{r})$  and  $w_R(\mathbf{r})$  the corresponding mean fields, and  $\xi(\mathbf{r})$  is the Lagrangian multiplier that enforces the incompressibility condition on the system. The free energy is a functional of these five functions and needs to be minimized with respect to each of these independent functions.

The single-chain partition function  $Q$  depends on the mean fields and can be calculated from

$$Q = \frac{1}{4\pi V} \int d\mathbf{r} d\mathbf{u} q(\mathbf{r}, \mathbf{u}, t=1) \quad (6)$$

The propagator  $q(\mathbf{r}, \mathbf{u}, t)$  satisfies the modified diffusion equation (MDE)<sup>34–36</sup>

$$\frac{\partial}{\partial t} q(\mathbf{r}, \mathbf{u}, t) = \left[ \frac{Na_R}{2\lambda_R} \nabla_{\mathbf{u}}^2 - Na_R \mathbf{u} \cdot \nabla_{\mathbf{r}} - w_R(\mathbf{r}) \right] q(\mathbf{r}, \mathbf{u}, t) \quad (7)$$

for  $0 \leq t \leq f$ , and

$$\frac{\partial}{\partial t} q(\mathbf{r}, \mathbf{u}, t) = \left[ \frac{Na_C}{2\lambda_C} \nabla_{\mathbf{u}}^2 - Na_C \mathbf{u} \cdot \nabla_{\mathbf{r}} - w_C(\mathbf{r}) \right] q(\mathbf{r}, \mathbf{u}, t) \quad (8)$$

for  $f < t \leq 1$ . The initial condition required for solving the propagator is  $q(\mathbf{r}, \mathbf{u}, 0) = 1$ .

Another propagator,  $q^*(\mathbf{r}, \mathbf{u}, t)$ , which is complementary to  $q(\mathbf{r}, \mathbf{u}, t)$  by starting from the  $t = 1$  terminal where  $q(\mathbf{r}, \mathbf{u}, 1) = 1$ , is needed due to the nonexchangeable labeling for the rod and coil blocks. It satisfies a similar MDE

$$\frac{\partial}{\partial t} q^*(\mathbf{r}, \mathbf{u}, t) = \left[ -\frac{Na_C}{2\lambda_C} \nabla_{\mathbf{u}}^2 - Na_C \mathbf{u} \cdot \nabla_{\mathbf{r}} + w_C(\mathbf{r}) \right] q^*(\mathbf{r}, \mathbf{u}, t) \quad (9)$$

for  $f < t \leq 1$ , and

$$\frac{\partial}{\partial t} q^*(\mathbf{r}, \mathbf{u}, t) = \left[ -\frac{Na_R}{2\lambda_R} \nabla_{\mathbf{u}}^2 - Na_R \mathbf{u} \cdot \nabla_{\mathbf{r}} + w_R(\mathbf{r}) \right] q^*(\mathbf{r}, \mathbf{u}, t) \quad (10)$$

for  $0 \leq t \leq f$ . The calculation propagates from the  $t = 1$  terminal.

Minimizing the free energy functional in eq 5 with respect to the functions  $\phi_C$ ,  $\phi_R$ ,  $\xi$ ,  $w_C$ , and  $w_R$ , we obtain

$$w_C(\mathbf{r}) = \chi N \phi_R(\mathbf{r}) + \xi(\mathbf{r}) \quad (11)$$

$$w_R(\mathbf{r}) = \chi N \phi_C(\mathbf{r}) + \xi(\mathbf{r}) \quad (12)$$

$$\phi_C(\mathbf{r}) + \phi_R(\mathbf{r}) = 1 \quad (13)$$

$$\phi_C(\mathbf{r}) = \frac{1}{4\pi Q} \int d\mathbf{u} \int_f^1 dt q(\mathbf{r}, \mathbf{u}, t) q^*(\mathbf{r}, \mathbf{u}, t) \quad (14)$$

and

$$\phi_R(\mathbf{r}) = \frac{1}{4\pi Q} \int d\mathbf{u} \int_0^f dt q(\mathbf{r}, \mathbf{u}, t) q^*(\mathbf{r}, \mathbf{u}, t) \quad (15)$$

Within SCFT, our task becomes solving eqs 6–15 self-consistently for given parameters.

The system requires solving MDEs for  $q(\mathbf{r}, \mathbf{u}, t)$  and  $q^*(\mathbf{r}, \mathbf{u}, t)$  that depend on three spatial variables for  $\mathbf{r}$ , two orientational variables for  $\mathbf{u}$ , and one time-like variable  $t$ . Various previous efforts<sup>25,31,32,37–43</sup> have been devoted to developing numerical algorithms to solve eqs 7 and 9 by means of reducing the number of involved variables of the systems according to the specific symmetry given by a physical problem. Here to deal with the full six-dimensional space, the recent numerical recipes developed by two of us<sup>20</sup> are exactly followed. Interested readers can refer to ref 20 for more details. In this work, the contour variable  $t$  is divided into 400 parts, a total number of  $64^3$  plane-wave bases were used for the spatial resolution, and a total of  $M = 121$  independent spherical harmonic bases were used for the orientational dependence (i.e., the maximum  $l$  in spherical harmonics considered is 10).

**2.2. Parameters in the Model.** The formalism presented in the last section is generally for wormlike–wormlike block copolymers with asymmetric persistence lengths and statistical segments, although we refer to one block as rod and the other as coil. There are a number of system parameters in the model. (a) The combination  $\chi N$  appears in the free energy (eq 5) and hence the mean fields (eqs 11 and 12). (b) The total volume fraction of the rod segment,  $f$ , is specified when eqs 7–10 are solved, and volume fractions are calculated from expressions 14 and 15. (c) The total number of segments along a chain,  $N$ , is needed in MDEs. (d) Two ratios,  $a_C/\lambda_C$  and  $a_R/\lambda_R$ , are shown in MDEs. (e) Assuming that one of the two length scales,  $a_C$  or  $a_R$ , can be used as the basic length scale to reduce  $\mathbf{r}$ , from the coupling term in eqs 7–10, we see that the ratio  $a_C/a_R$  is an independent parameter. In this section, we identify the independent parameters for the rod–coil system specifically. The parameters in (a) and (b) are basic parameters that are kept independent in the theory.

For the coil segment, we understand that the effective Kuhn length, which is taken as  $a_C$  here, is related to  $2\lambda_C$  in a long polymer on the basis of the mean-square end-to-end distance in free space.<sup>29</sup> We take

$$a_C/2\lambda_C = 1 \quad (16)$$

in this paper. For the rod segment, the persistence length  $\lambda_R \gg L$ . Then, we have

$$a_R/\lambda_R = 0 \quad (17)$$

which directly makes the first terms in the square brackets of eqs 7 and 10 disappear. Allowing  $\mathbf{r}$  to be reduced by  $Na_R$ , these two equations depend on  $w_R$  directly. For a rod–coil theory, parameters in (d) on the above list hence vanish.

The MDE for the coil block, in the form of eqs 8 and 9, then contains  $N$  (first term) and  $a_C$  (second term) as adjustable parameters. Two of us have recently shown that within the coil limit at a moderate external field, i.e.,  $N \gg 1$ ,  $W \sim \sqrt{N} a_C$  and  $\chi N \sim N^0$  where  $W$  is a typical interfacial width, the WLC MDE (eq 8) completely reduces to GSC MDE<sup>20</sup>

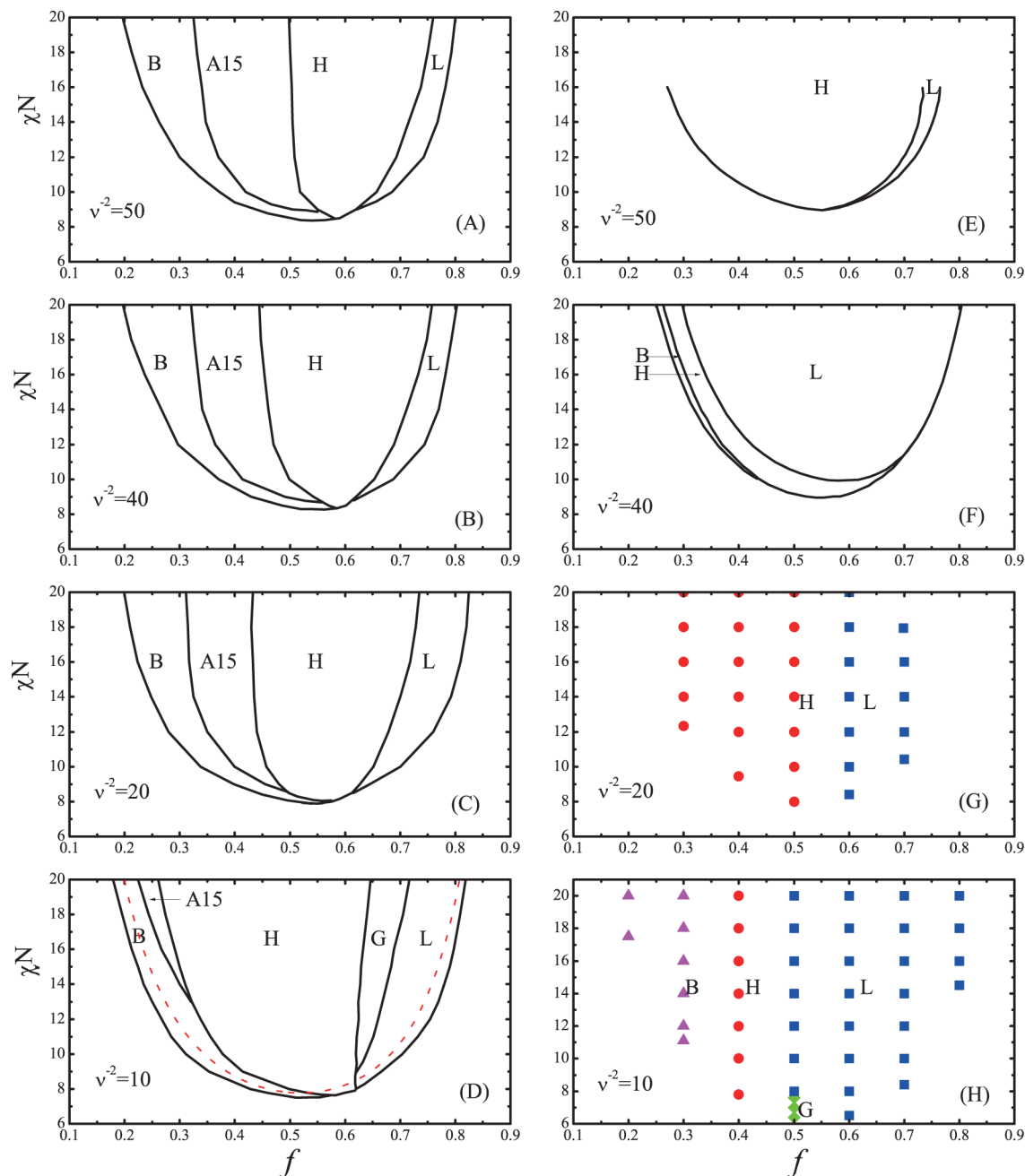


**Figure 2.** Phase diagram of rod–coil diblock copolymer melts calculated in the current work in terms of  $\chi N$  and  $f$  for (A)  $\nu^{-2} = 50$ , (B) 40, (C) 20, and (D) 10. Stability regions for B (body-centered cubic spheres), A15 (A15 spheres), H (hexagonal cylinders), G (gyroid phase), L (lamellar phase), and D (disordered phase) are separated by first-order phase boundaries. Phase diagrams determined from previous work are shown for comparison: (E)  $\nu^{-2} = 50$ ,<sup>16</sup> (F)  $\nu^{-2} = 40$ ,<sup>24</sup> (G)  $\nu^{-2} = 20$ ,<sup>28</sup> and (H)  $\nu^{-2} = 20$ .<sup>26</sup> The red dashed line in (D) is the spinodal line calculated from the random phase approximation.

$$\frac{\partial}{\partial t} q_0(\mathbf{r}, s) = \frac{Na_C^2}{6} \nabla_{\mathbf{r}}^2 q_0(\mathbf{r}, s) - w_C(\mathbf{r}) q_0(\mathbf{r}, s) \quad (18)$$

where  $q_0(\mathbf{r}, t)$  is the orientationally averaged WLC propagator. Taking the same reduction for  $\mathbf{r}$ , we then see the coefficient of the  $\nabla$  term is an independent combination of parameters

$$Na_C^2/6 \times (Na_R)^{-2} = (a_C/a_R)^2/6N \equiv \nu^2/6 \quad (19)$$

which is the same rod–coil asymmetric parameter identified in refs 17, 22, and 25. Hence,  $\nu^2 = (a_C/a_R)^2/N$  is an independent parameter.

For a flexible block that can be described by a Gaussian-chain model (hence eq 18),  $N$  only shows up within  $\nu$  together with the ratio  $a_C/a_R$ . Therefore, there are only three parameters:  $\chi N$ ,  $f$ , and  $\nu$ . The calculation in this work is actually carried out by solving the WLC model (through eqs 8 and 9) where  $N$  and  $a_C/a_R$  show up in separate places. Strictly speaking, we have four parameters in the theory:  $\chi N$ ,  $f$ ,  $N$ , and  $\nu$ . Within the large- $N$  range we explore, the coil block is in the flexible region; therefore, we are essentially solving eq 18 but using a different method. Letting  $a_C/a_R = 1$  in this calculation, which leads to  $\nu = 1/\sqrt{N}$ , the results should be no different from those obtained by solving eq 18. We examined systems with  $N = 10, 20, 40$ ,

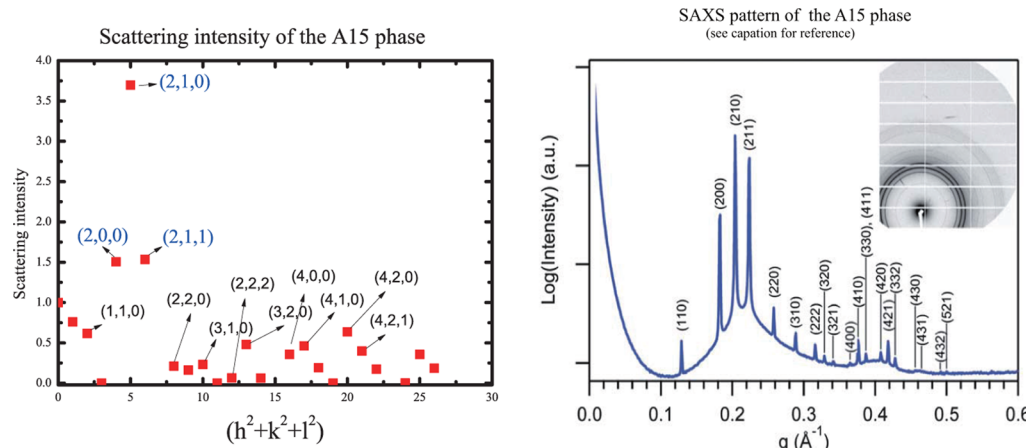


**Figure 3.** Spectrum analysis of the A15 state stabilized at  $\chi N = 20$ ,  $\nu^{-2} = 50$ , and  $f = 0.36$ . The left panel is the scattering intensity simulated from the density profile produced from the current calculation, where the scattering peaks are labeled by the reciprocal lattice vector indexes ( $h, k, l$ ); the right panel is a reproduction of a real A15 spectrum from an experiment, reported in Figure 1 of ref 50.

and 50. The results in this work are therefore presented in terms of parameters  $\chi N$ ,  $f$ , and  $\nu$ .

### 3. RESULTS AND DISCUSSION

**3.1. Phase Diagram.** Most previous SCFT studies of rod-coil diblock melts only handle polymer models that describe one-dimensional or two-dimensional (2D) spatial variations.<sup>17,22,44,45</sup> The reduction of dimensionality made the calculation simpler than a full three-dimensional (3D) treatment. Recently, a massively parallel 3D SCFT scheme, in which a polymer is modeled by a rod block connected to a Gaussian coil, was proposed by Kriksin and Khalatur.<sup>23</sup> They demonstrated the usefulness of high-resolution 3D calculation for specific points in the parameter space.<sup>23</sup> Our WLC formalism and the algorithm presented in ref 20 allow us to tackle a 3D calculation for the rod-coil system rather easily, on a single computer node consisting of, for example, 32 CPU cores. This enables us to explore a significant range of parameters.

We first present the rod-coil phase diagrams at  $\nu^{-2} = 50$ , 40, 20, and 10 in Figure 2. The sequence of ordered phases  $B \rightarrow H \rightarrow G \rightarrow L$  as  $f$  varies in the range  $[0, 1]$  is the same as the sequence found in coil-coil diblock copolymer melts for  $f$  in the range  $[0, 1/2]$ . All structures contain a highly packed rod-rich region inside the convex surface shown in Figure 2. In comparison with the coil-coil diblock copolymer phase diagram,<sup>46</sup> the B, H, and G phases expand into a much larger phase region. The L phase now has a narrower size and is shifted toward a larger  $f$  region.

The rod-coil phase diagram is no longer symmetric about  $f = 0.5$ ; the latter is a typical property of diblock copolymers with the same persistence lengths. This is caused by the fundamental difference between the architecture of the two blocks constituting the copolymers. Bates et al. pointed out that there are two kinds of symmetries in diblock copolymer melts: the compositional symmetry and the conformational symmetry.<sup>47</sup> Both are needed for a symmetric phase diagram. On the basis of a Landau theory, Leibler predicted a critical point of microphase separation at  $\chi N = 10.495$ ,  $f = 0.5$  for a compositionally and conformationally symmetric flexible diblock melts.<sup>13</sup> Using the random-phase approximation, Zhang et al. calculated the critical point of microphase separation for semiflexible-semiflexible diblock copolymers with the same

persistence lengths; the critical point is located at the compositionally symmetric point  $f = 0.5$  for a critical  $\chi N$  that now depends on the chain flexibility.<sup>48</sup> In these systems the free energy expansion is an even function of an order parameter; hence, a critical point exists. In contrast, rod-coil diblock copolymers lack the conformational symmetry. The free energy is not invariant when the two rod and coil blocks interchange their volume fractions, whereas in a conformationally symmetric diblock polymer, the free energy is invariant with such an interchange. A microphase separation critical point hence does not exist in a rod-coil melt.

Nevertheless, the stability limit of the disorder state can still be examined by determining a spinodal curve. The determination of the structural factor and the use of the random phase approximation enable the calculation of such a curve for the rod-coil melt.<sup>49</sup> The red curve in Figure 2D represents this stability limit. The disorder-to-order transition is now discontinuous over the entire range  $0 \leq f \leq 1$ . Typical of a first-order transition, the spinodal line is above the binodal (phase boundary) line. A disorder structure that runs into the region between the binodal and spinodal lines is metastable.

The A15 sphere phase has been observed experimentally and determined theoretically in systems such as supramolecular dendrimers and  $AB_n$  miktoarm block copolymers.<sup>51–58</sup> Using geometric argument, Grason et al.<sup>55</sup> pointed out that the Voronoi cell of A15 lattice has the minimal interfacial area for partitioning 3D periodic AB structures, which is also known as the Weaire and Phelan lattice partition in discrete geometry.<sup>59</sup> The stability of A15 of rod-coil copolymers is first predicted here in the large  $\nu^{-2}$  regime.

The A15 sphere phase we discovered in our SCFT calculation is a nonconventional structure in diblock copolymer self-assembly. Beyond visual inspection of the A15 structure, we perform a spectrum analysis simulated from our SCFT calculation to further identify the A15 phase. The amplitudes of the Fourier transformation of the density profile for the A component is identified, shown in Figure 3a, in a similar way discussed for other structures by Erkumovich et al.<sup>60,61</sup> The plot is consistent with a real XRD pattern obtained experimentally, shown in plot (b). The three dominant Bragg peaks with the reflection indexes (2, 0, 0), (2, 1, 0), and (2, 1, 1) are unique to an A15 phase.

The emergence of the G state is between  $\nu^{-2} = 20$  and 10, also confirmed here for the first time. The bicontinuous gyroid structure can be exploited to create nanoporous materials. The gyroid nanostructure is a good template for applications such as photonic crystals, antireflection structures, and hybrid solar cells.<sup>62–65</sup> In contrast, the gyroid structure only exists in a narrow phase region, first discovered by Thomas et al.<sup>66</sup> for flexible–flexible copolymers.

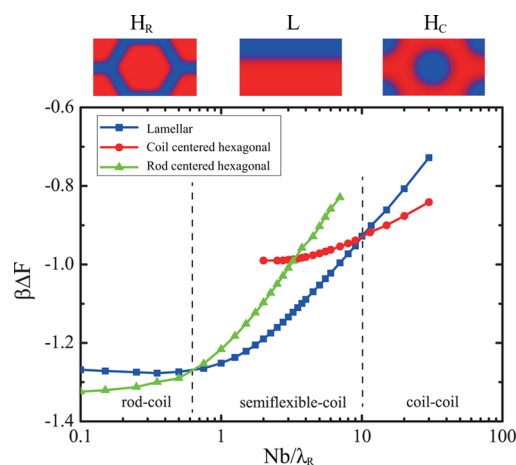


**Figure 4.** Examples of the reduced free energy per chain  $\beta\Delta F$  by taking the free energy of the disordered state  $F_D$  as the reference,  $\Delta F = F - F_D$ . In particular, we examine a system with  $\chi N = 20$ ,  $f = 0.65$ , and  $\nu^{-2} = 10$  (the B block is flexible). The flexibility of the A block is continuously tuned from  $N\alpha_R/\lambda_R = 0.1$  (rod-like) to  $N\alpha_R/\lambda_R = 30$  (flexible). The influence of  $N\alpha_R/\lambda_R$  on the stability of three structures, rod-centered hexagonal ( $H_R$ ), lamellar ( $L$ ), and coil-centered hexagonal ( $H_C$ ), is determined by the free energy curves. The structures are illustrated on the top of the figure where the rod-rich and coil-rich domains are plotted by red and blue colors, respectively.

As an ending note, we have searched the parameter space with initial assumptions that contain various symmetries known to exist on the coil–coil phase diagram. This includes cubic and orthorhombic unit cells with plausible candidate phases such as *Fddd* or *FCC*, etc., in addition to random initial conformations. Both *Fddd* and *FCC* are found metastable. No other structures beyond those illustrated in Figure 1 were found stable. Of course, we cannot claim that we have performed an exhaustive search based on all known crystallographic structures.

**3.2. Comparison with Previous Studies.** In Figure 2E–H, we reproduced four previous rod–coil phase diagrams, reading data off from the original publications.<sup>16,24,26,28</sup> Although these phase diagrams were produced from different chain models or theoretical tools, in the parameter region considered, our model and these results should have yielded the same results.

Müller and Schick produced Figure 2E, using the weak- and strong-segregation theories to determine the phase boundaries between H, L, and D phases.<sup>16</sup> The large H phase region and the small L phase region they predicted are in good agreement with the approximate size and location of the same phases in the current study presented in Figure 2A.

Using the Landau free energy expansion, Reenders and ten Brinke obtained the phase diagram in Figure 2F for  $\nu^{-2} = 40$ , which contains a rather large L region, different from the general trend present in the phase diagrams by Müller and Schick<sup>16</sup> as well as Li and Gersappe<sup>24</sup> (see Figure 2E,G). Our

calculation for  $\nu^{-2} = 40$  as presented in Figure 2B is consistent with these two references but disagrees with Figure 2F.

Li and Gersappe produced Figure 2G for  $\nu^{-2} = 20$  on the basis of a 2D self-consistent-field lattice model.<sup>28</sup> Clearly, it has a similar phase-diagram structure to Figure 2A, but the L state occupies a larger phase region. The general features of the phase diagram agree with our calculation shown in Figure 2C, where the B phase is now stable in the small  $f$  regime.

An interesting comparison of this study is the 3D lattice SCFT calculation performed by Chen et al.,<sup>26</sup> who also adopted  $\nu^{-2} = 20$ . In Figure 2H, the L phase dominates a large region. For the first time, they suggested the existence of the G phase near the  $f = 0.5$  at the bottom of the disorder–order boundary. Our calculation shows that the G phase is only metastable for  $\nu^{-2} = 20$  but stable for  $\nu^{-2} = 10$ .

Overall, from the left to right, the sequence of B, H, G, and L is mostly kept in all these phase diagrams, but the phase regions differ. From Figure 2E–G to Figure 2D, the choice of  $\nu^{-2}$  is 50, 40, 20, and 10. The phase diagrams can differ, but different features should evolve consistently. The emergence of the G state is between  $\nu^{-2} = 20$  and 10.

From the above discussion, we see that there has not been a common understanding on the rod–coil phase diagrams as a function of  $\nu$ . This could be attributed to the difference in modeling techniques and the inaccuracy of numerical calculation for the free energy. The latter is particularly important as the phase boundary is usually determined by a small free energy difference.

As a final note, the bottom of the order-to-disorder transition point can be examined from these figures. From previous work, ranging from  $\nu^{-2} = 50$  (in Figure 2a), 40 (in Figure 2b), and 20 (in Figure 2c), we observe the location of  $\chi N = 9.2$  ( $\nu^{-2} = 50$ ), 9.0 ( $\nu^{-2} = 40$ ), and 8.0 ( $\nu^{-2} = 20$ ) from (c). The only one that is quite different from this sequence is  $\chi N = 6.5$  ( $\nu^{-2} = 20$ ) from (d). In comparison, from the present work, the locations of the bottom of the order-to-disorder transition points are  $\chi N = 8.3$  ( $\nu^{-2} = 50$ ),  $\chi N = 8.2$  ( $\nu^{-2} = 40$ ),  $\chi N = 7.9$  ( $\nu^{-2} = 20$ ), and  $\chi N = 7.4$  ( $\nu^{-2} = 10$ ).

It is worth noting that the rod–coil phase diagram resembles that of a conformational asymmetric coil–coil diblock melt (flexible diblock copolymers with block A and B, having a different Kuhn segments length  $a_A$  and  $a_B$ ). Matsen and Schick<sup>67</sup> as well as Vavasour and Whitmore<sup>68</sup> focused on the change of phase diagrams induced by the conformational asymmetry. For an asymmetric case of  $a_A/a_B = \sqrt{10}$ , the phase regions with A blocks forming the minority domain are much wider than those formed by minority B blocks.<sup>68</sup> Such similarities between rod–coil and conformationally asymmetric coil–coil melts are not surprising because both contain a relatively rigid A block.

**3.3. Inverted Structures.** A noticeable feature of a rod–coil melt is the lack of stable inverted structures, usually seen in the  $1/2 \leq f \leq 1$  phase region of a coil–coil melt. These are the H, G, and B structures where inside the convex surface the space is packed with coil-rich domains. This is consistent with the discussion of Müller and Schick<sup>16</sup> as well as Kriksin and Khalatur<sup>23</sup> for the parameter region explored in their rod–coil systems. In contrast, coil–coil copolymer systems with conformationally asymmetric chain architecture, such inverted morphologies where the longer blocks segregate into the micelles interior were previously discovered.<sup>69,70</sup>

The formalism presented in section 2 is generally set up for a conformationally asymmetric semiflexible–semiflexible melt.

To further demonstrate the disappearance of the inverted structure in a rod–coil system, we varied  $N\alpha_R/\lambda_R$  of the so-called rod block from 0 (rod–coil copolymer) to a large number (coil–coil copolymer) to explore the free energy landscape, at  $\chi N = 20$ ,  $f = 0.65$ , and  $\nu^{-2} = 10$ . The coil block is a minority component at this  $f$ . At a large  $N\alpha_R/\lambda_R$  when both blocks are flexible, the inverted H phase has the lowest energy hence is stable; this is typically observed in a coil–coil melt. In the middle range of  $N\alpha_R/\lambda_R$ , the rod block becomes semiflexible, and the copolymer is essentially a semiflexible–coil polymer. It is this region where L phase takes over. Within the low  $N\alpha_R/\lambda_R$  range, the semiflexible block becomes rigid. Then, the rod-centered H phase becomes stable.

This interesting phase behavior is caused by the packing frustration effect in rod–coil diblock system, which we will discuss next.

### 3.4. Interfacial Curvature and Packing Frustration.

The basic mechanism of diblock copolymer self-assembly is the competition between the interfacial tension created by the enthalpic penalty of mixing two blocks, which prefers minimizing the interfacial area, and the entropic penalty of chain deformation, which prefers maximizing interfacial area. Matsen and Bates noted that packing frustration caused by the incompressibility condition is equally important.<sup>71</sup> To accommodate enthalpic and entropic requirements while minimizing packing frustration, the domain interface must be altered to display a nonconstant curvature.

In coil–coil AB diblock copolymer melts, the interfacial area is mainly minimized by the interfacial tension. As such for a system with a volume constraint, the surface prefers a constant mean curvature (CMC). Simultaneously, the system must minimize packing frustration to remain incompressible; this leads to a relatively uniform thickness so as to equally distribute the local entropic penalties. As a result, the majority blocks outside the interface must be stretched excessively to fill the Voronoi cell. An example is the hexagonal structure; extensive stretching of the majority blocks toward the six corners of the unit cell is required, which leads to a nonconstant curvature. In a rod–coil system, packing frustration was discussed in refs 71–73, and minimizing of packing frustration was shown to be particularly important by experiments in triblock copolymers.<sup>74</sup>

In the current rod–coil system, we find that packing frustration is even more profound than that in a coil–coil system. At  $\chi N = 15$  the hexagonal structure is stable over a relatively large range in  $f$  for  $\nu^{-2} = 10$ . Taking a cross-section plot of the structure, we can measure the distance from the interfacial surface (where  $\phi_R = 0.5$ ) to the center of the rod-rich domain,  $R(\theta)$ , where  $\theta$  is the polar angle defined on cross-section plane. This function is then fitted to the formula

$$R(\theta) = \langle R \rangle [1 - \delta \cos(6\theta)] \quad (20)$$

where two constants are determined: the mean interfacial radius,  $\langle R \rangle$ , and the deviation from CMC,  $\delta$ .<sup>72</sup> Both quantities are plotted in Figure 5. At large  $f$ , the rod-rich domain (in red) forms a honeycomb-like hexagonal shape with clear six corners. The measurement  $\delta$  reaches a high value. As  $f$  decreases,  $\delta$  rapidly decreases as well. Eventually, once  $f \lesssim 1/2$ , the rod-rich domain displays a cylinder shape with more uniform radius variation.

To further demonstrate the properties of packing-frustrated induced nonconstant interfacial curvature, in Figure 6, we plot

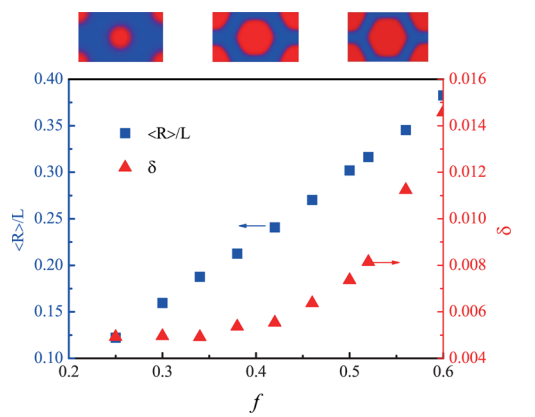


**Figure 5.** Reduced average radius,  $\langle R \rangle / L$ , and the deviation from CMC,  $\delta$ , as functions of  $f$  for  $\chi N = 15$  and  $\nu^{-2} = 10$ . Three typical density profiles for  $f = 0.3$ ,  $0.5$ , and  $0.6$  are shown on the top of the figure (rod and coil blocks are displayed in red and blue).

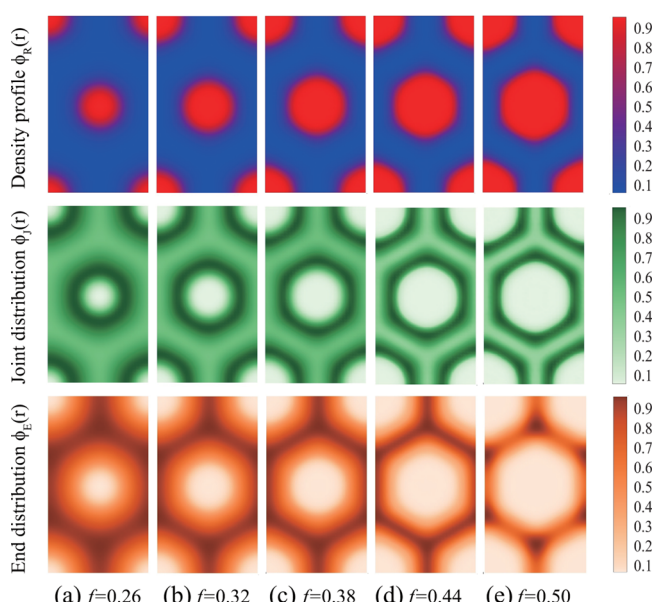


**Figure 6.** Density plots for the rod-rich (red) and coil-rich (blue) blocks, rod–coil joint-point distribution (green)  $\phi_J(r)$ , and coil end-point distribution (orange)  $\phi_E(r)$  for different  $f$  at  $\chi N = 16$  and  $\nu^{-2} = 50$ .

the density profile of rod block  $\phi_R(r)$ , the distribution function of the rod–coil joint points

$$\phi_J(r) = \frac{1}{4\pi Q} \int d\mathbf{u} q(\mathbf{r}, \mathbf{u}, f) q^*(\mathbf{r}, \mathbf{u}, f) \quad (21)$$

and the distribution function of the coil ends

$$\phi_E(r) = \frac{1}{4\pi Q} \int d\mathbf{u} q(\mathbf{r}, \mathbf{u}, 1) \quad (22)$$

At  $f = 0.26$  (see Figure 6a), the rod-rich domain forms a cylinder with an approximately constant curvature. This can be understood from the fact that as the rod volume fraction is relatively small, the rod-rich domains are far away from each other. The coil ends are distributed uniformly outside the domains; thus to minimize the interfacial energy, a round interface is formed in low  $f$ . In contrast, at  $f = 0.50$ , the system displays a sharper interface with a honeycomb-like morphology.

The rod-rich domain expands significantly, and this causes a serious packing problem. To meet the incompressible condition and to keep a relatively uniformly thickness of the coil-rich domain, the coil blocks must be aggressively stretched to fill the interstitial voids<sup>73</sup> in order to maintain a constant monomer concentration. According to Figure 6e, coil ends are now mostly located at the six corners of the honeycomb wall, which is a direct sign of overstretching of the coil blocks. The entropy is unfavorably lowered because of the packing frustration. The H state eventually yields to the L state at a high  $f$ .

Below we present a similar analysis for the B and A15 phases by visualizing the shape evolution of the rod-coil interface as the rod volume fraction  $f$  increases at  $\chi N = 16$  and  $\nu^{-2} = 50$ . At  $f = 0.26$ , the rod-rich domains are relatively small and far from each other; the interfaces of the B and A15 phases are both insensitive to their polyhedral environment of the Voronoi cell, displaying approximatively spherical shapes. This can be viewed from the uniform color map in Figure 7a, which shows that the

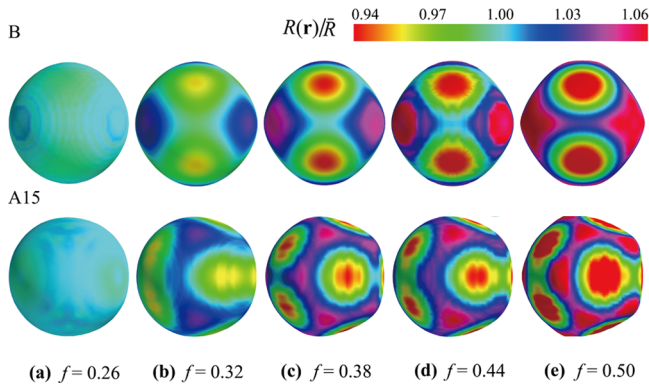


**Figure 7.** Interface shapes of the center spheres of B and A15 states, determined by  $\phi_R(\mathbf{r}) = 0.5$ , for different  $f$  at  $\chi N = 16$  and  $\nu^{-2} = 50$ . The surfaces are colored according to  $R(\mathbf{r})/\bar{R}$ , where  $R(\mathbf{r})$  is the surface distance from the center and  $\bar{R}$  is the average. The interfacial area ratio,  $A^{A15}/A^B$ , has the value (a) 0.9986, (b) 0.9930, (c) 0.9808, (d) 0.9667, and (e) 0.9501.

influence of packing is at its minimum. As  $f$  increases, the rod-rich domains expand into a much larger size and different domains start to affect each other.

To meet the incompressibility condition and relieve the packing frustration, the rod-rich spheres deform into a polyhedral shape accommodating the geometry of the corresponding Voronoi cell. To quantitatively characterize the deformation of the interface, we measure the distance from the rod-rich domain center to the surface,  $R(\hat{\mathbf{r}})$ . A mean curvature  $\bar{R}$  is then produced based on average over the 3D angular direction,  $\hat{\mathbf{r}}$ . The distribution of  $R(\hat{\mathbf{r}})/\bar{R}$  is visualized by a color scheme on the interface. As  $f$  increases, the interface changes its shape from an approximately uniform sphere to a Voronoi cell. Further study indicates that the gap between the blue regions of the neighboring rod-rich domains is also where the coil ends are mostly concentrated. The gap between the red regions of the neighboring rod-rich domains contains less coil ends. Hence, the coil blocks are stretched into specific 3D domains, losing their entropy to accommodate packing. To quantitatively demonstrate the interface areas in both B and A15 phases, we calculated

$$A \equiv \int d\mathbf{r} \phi_R(\mathbf{r})\phi_C(\mathbf{r}) \quad (23)$$

as an effective measure. This quantity is essentially the Flory-Huggins energy, without the  $\chi$  parameter. In the caption of Figure 7, we list the effective area of A15 and B states,  $A^{A15}/A^B$ . The interface is reduced relatively as  $f$  increases at large packing frustration, which eventually drives the B-A15 phase transition.

Finally, packing requirement can also be used to explain why a lamellar structure is found stable at a relatively large value of  $f$ . According to the illustration in Figure 8, at a small value of  $f$ ,

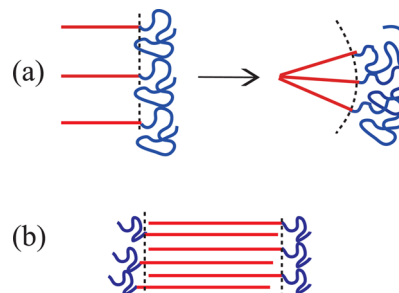


**Figure 8.** Schematic illustration of packing rod-coil diblock copolymers.

the coil blocks must be strongly compressed to minimize packing frustration, which produces a large entropy penalty. Therefore, as a compromise, an interface with a spontaneous curvature is favored so that the coil blocks outside can be relaxed to relieve packing frustration. On the other hand, at a large  $f$ , packing frustration in the L structure is much reduced; hence it becomes stable.

**3.5. Interfacial Width.** Now we turn our attention to the interfacial width  $W$ , defined by<sup>19,32</sup>

$$W = [\max|\nabla_{\mathbf{r}}\phi_R(\mathbf{r})|]^{-1} \quad (24)$$

This definition characterizes a typical length scale on which the density profile varies most drastically. It recovers the definition for a planar interfacial width.<sup>75</sup> Qualitatively, for microphase separation,  $W^{-1}$  can be viewed as an order parameter. At a first-order phase transition boundary,  $W^{-1}$  jumps abruptly from the measure in one phase to another.

Figure 9 displays both  $\Delta F$  and  $W^{-2}$  as a function of  $(\chi N - \chi^*N)$ , where  $\chi^*N$  is the transition point at a specific  $f$ , from the ordered phase to a disordered phase, for  $\nu^{-2} = 10$ . Four separate sets of data are examined:  $f = 0.2$  (B-D transition),  $f = 0.52$  (B-D transition),  $f = 0.6$  (H-D transition), and  $f = 0.7$  (L-D transition). In the first and last cases,  $f = 0.2$  and  $f = 0.7$ , we clearly observe a finite jump in  $W^{-2}$  at the transition points and the linear behavior of  $\beta\Delta F$  approaching the transition points. These are signatures of a first-order phase transition.

In both  $f = 0.5$  and  $f = 0.6$  cases, however, the first-order phase transition signatures become much weaker. In particular, the gaps of  $W^{-2}$  at the transition points now become almost invisible between the ordered and disordered phases, shown in the middle two plots of Figure 9. However, in Figure 2D, we can observe that the spinodal curve is clearly inside the binodal curve.

To further demonstrate the first-order nature of the transition near the bottom of the binodal curve, we plot the difference between the spinodal and binodal curves,  $\Delta\chi_{sb}N = (\chi_{spinodal} - \chi_{binodal})N$  and the transition gap of  $W^{-1}$  at the transition point, as functions of  $f$  for  $\nu^{-2} = 10$ . As can be seen from Figure 10, near  $f = 0.5$ , both quantities decrease but

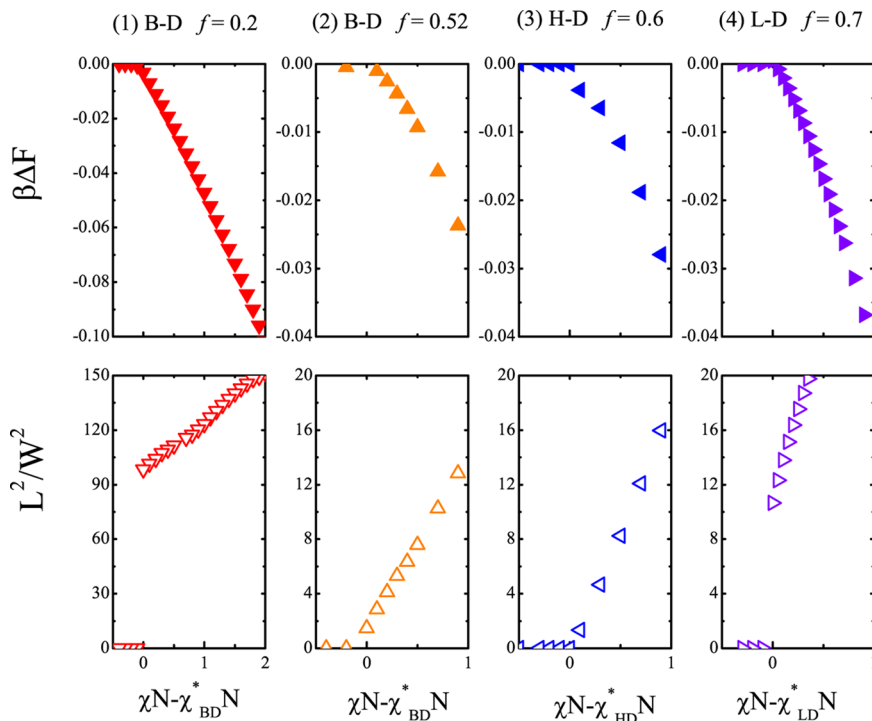


**Figure 9.** Numerical result of the reduced free energy difference  $\beta\Delta F$  between an ordered phase (B, H, L) and the disordered phase (D) near the phase transition points (upper panels), and the inverse square interfacial width  $W^{-2}$  (lower panels) as functions of  $\chi N - \chi^* N$  for  $\nu^{-2} = 10$ . At the disorder-to-order transition point, we have  $\chi_{BD}^* N = 16.1$  ( $f = 0.2$ ),  $\chi_{BD}^* N = 7.5$  ( $f = 0.52$ ),  $\chi_{HD}^* N = 7.8$  ( $f = 0.6$ ), and  $\chi_{LD}^* N = 9.7$  ( $f = 0.7$ ).

remain at a finite value. At a second-order transition, these gaps would have to be closed.

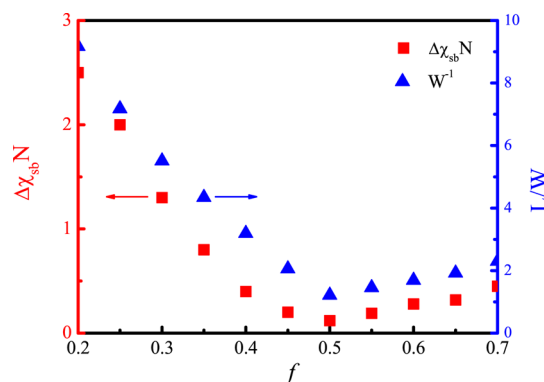


**Figure 10.** Gap between the binodal and spinodal curves,  $\Delta\chi_{sb}N$  (to the left scale), and the inverse interfacial width,  $W^{-1}$  (to the right scale), as a function of  $f$  at the order-to-disorder transition points for  $\nu^{-2} = 10$ .

**3.6. Orientational-Ordering Map.** The WLC formalism has a distinctive feature of being able to deal with the orientational ordering directly. In the current problem the immiscible interaction between rod and coil components drives domain separation in the system. Even without the orientational interaction, the rod blocks already display an orientational ordering at the interfacial area between rod-rich and coil-rich domains. To visualize the orientational order, we define an average vector field, adopted from previous studies of related systems.<sup>20,27</sup>

$$\langle \mathbf{u}(\mathbf{r}) \rangle = \frac{1}{4\pi Q} \int d\mathbf{u} \mathbf{u} \int_0^f ds q^\dagger(\mathbf{r}, \mathbf{u}, s) q(\mathbf{r}, \mathbf{u}, s) \quad (25)$$

As a function of position, such a vector field illustrates the local orientation direction the rod blocks. In Figure 11, we present the orientational ordering map along with the interfacial density profile by sectional drawings. We demonstrate here that orientational ordering can be induced by the immiscibility interaction alone. The rod blocks in an L state are aligned parallel to each other, leading to a nematic order. In other more complicated structures, rods are observed to align in a direction parallel to the interfacial normal direction.

#### 4. SUMMARY

Using SCFT, we study the structure of incompressible rod-coil diblock copolymer melts on the basis of the wormlike-chain model. We focus on microphase separation driven by the Flory-Huggins interaction. Under this assumption we construct a mean-field phase diagram that contains the classical lamellar, hexagonal, gyroid, and body-centered cubic (bcc) phases, as well as the emergent A15 phase, by systematically varying the asymmetric parameter. In comparison with that of coil-coil AB diblocks, the phase diagram is highly asymmetric on the compositional fraction  $f$ . In the present system, the inverted structures with coil blocks inside the convex interface are completely absent, and the phase regions of bcc, hexagonal, and gyroid are all shifted to a higher rod volume fraction and are expanded. Notably, the rod centered hexagonal phase have the largest domain area on the ordered phase region. The stability of A15 is enhanced as the conformational asymmetry increases. The stable region of the lamellar phase is suppressed and shifted toward a relatively large compositional fraction of rod ( $f > 0.6$ ). The spinodal line is plotted on the phase diagram which is now asymmetric about  $f$ . Combined with the binodal

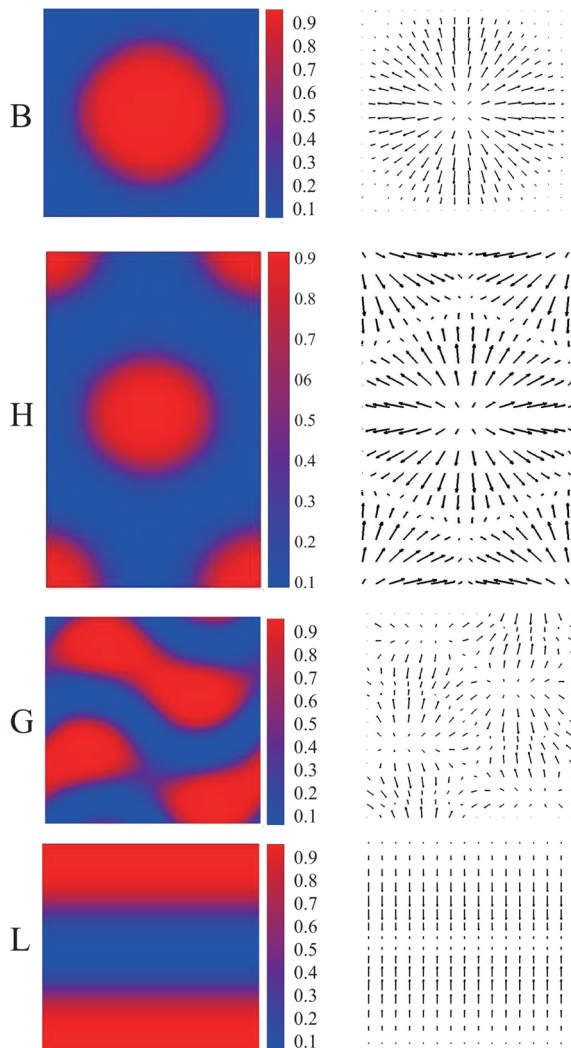


**Figure 11.** Orientation map of the rod blocks for the B, H, G, and L phases in a cross-section view. The structures were selected from parameter points at  $\chi N = 16$ ,  $\nu^{-2} = 10$ , and  $f = 0.25, 0.3, 0.65, 0.7$ , respectively. The four figures on the left are density plots of rod blocks, ranging from high (red) to low (blue). The four figures on the right illustrate the local preferred direction of rod blocks, where an arrow represents the averaged  $\mathbf{u}$  direction and the length of the arrow represents the magnitude of  $\langle \mathbf{u} \rangle$ .

curve, we find that the order-disorder transition curve in full range of  $f$  is of the first order, and this first-order characteristic is also demonstrated by the finite jump of interfacial width at the phase transition point.

Another interesting feature is that packing frustration plays an important role in the rod-coil diblock melts. The shape of the rod-coil domain interface is observed to have a spontaneous nonconstant curvature as  $f$  or  $\chi N$  increases. Our result suggests that the nonconstant curvature is a direct result of geometry frustration to pack the coil blocks into a Voronoi cell.

## AUTHOR INFORMATION

### Corresponding Authors

\*E-mail: [yandd@bnu.edu.cn](mailto:yandd@bnu.edu.cn) (D.Y.).

\*E-mail: [jeffchen@uwaterloo.ca](mailto:jeffchen@uwaterloo.ca) (J.Z.Y.C.).

### Notes

The authors declare no competing financial interest.

## ACKNOWLEDGMENTS

We thank financial support from the National Science Foundation Research of China (NSFC) 21374011, 21434001, 21204067, 21304008, 21574006, the 973 Program of the Ministry of Science and Technology (MOST) 2011CB808502, the Fundamental Research Funds for the Central Universities 30404101, the SRF for ROCS, SEM, and Natural Sciences and Engineering Research Council of Canada (NSERC).

## REFERENCES

- Bates, F. S.; Hillmyer, M. A.; Lodge, T. P.; Bates, C. M.; Delaney, K. T.; Fredrickson, G. H. *Science* **2012**, *336*, 434.
- Coakley, K. M.; McGehee, M. D. *Chem. Mater.* **2004**, *16*, 4533–4542.
- Günes, S.; Neugebauer, H.; Sariciftci, N. S. *Chem. Rev.* **2007**, *107*, 1324.
- Segalman, R. A.; McCulloch, B.; Kirmayer, S.; Urban, J. J. *Macromolecules* **2009**, *42*, 9205.
- Olsen, B. D.; Segalman, R. A. *Mater. Sci. Eng., R* **2008**, *62*, 37–66.
- Chen, J. T.; Thomas, E. L.; Ober, C. K.; Mao, G. P. *Science* **1996**, *273*, 343.
- Chen, J. T.; Thomas, E. L.; Ober, C. K.; Hwang, S. S. *Macromolecules* **1995**, *28*, 1688.
- Jenekhe, S. A.; Chen, X. L. *Science* **1999**, *283*, 372.
- Ryu, J. H.; Oh, N. K.; Zin, W. C.; Lee, M. *J. Am. Chem. Soc.* **2004**, *126*, 3551.
- Lim, Y. B.; Moon, K. S.; Lee, M. *J. Mater. Chem.* **2008**, *18*, 2909.
- Hoeben, F. J. M.; Jonkheijm, P.; Meijer, E. W.; Schenning, A. P. H. *J. Chem. Rev.* **2005**, *105*, 1491.
- Shi, L. Y.; Zhou, Y.; Fan, X. H.; Shen, Z. *Macromolecules* **2013**, *46*, 5308.
- Leibler, L. *Macromolecules* **1980**, *13*, 1602.
- Matsen, M. W.; Schick, M. *Phys. Rev. Lett.* **1994**, *72*, 2660.
- Ranjan, A.; Qin, J.; Morse, D. C. *Macromolecules* **2008**, *41*, 942.
- Müller, M.; Schick, M. *Macromolecules* **1996**, *29*, 8900.
- Matsen, M. W.; Barrett, C. *J. Chem. Phys.* **1998**, *109*, 4108.
- Shah, M.; Pryamitsyn, V.; Ganesan, V. *Macromolecules* **2008**, *41*, 218.
- Jiang, Y.; Chen, J. Z. Y. *Phys. Rev. Lett.* **2013**, *110*, 138305.
- Jiang, Y.; Chen, J. Z. Y. *Phys. Rev. E* **2013**, *88*, 042603.
- Maier, W.; Saupe, A. Z. *Naturforsch., A: Phys. Sci.* **1958**, *13*, 564.
- Pryamitsyn, V.; Ganesan, V. *J. Chem. Phys.* **2004**, *120*, 5824.
- Kriksin, Y. A.; Khalatur, P. G. *Macromol. Theory Simul.* **2012**, *21*, 382.
- Reenders, M.; ten Brinke, G. *Macromolecules* **2002**, *35*, 3266.
- Gao, J.; Tang, P.; Yang, Y. *Soft Matter* **2013**, *9*, 69.
- Chen, J. Z.; Zhang, C. X.; Sun, Z. Y.; Zheng, Y. S.; An, L. J. *J. Chem. Phys.* **2006**, *124*, 104907.
- Li, S.; Jiang, Y.; Chen, J. Z. Y. *Soft Matter* **2014**, *10*, 8932.
- Li, W.; Gersappe, D. *Macromolecules* **2001**, *34*, 6783.
- Saito, N.; Takahashi, K.; Yunoki, Y. *J. Phys. Soc. Jpn.* **1967**, *22*, 219.
- Flory, P. J. *Principles of Polymer Chemistry*; Cornell University Press: Ithaca, NY, 1953.
- Matsen, M. W. *J. Chem. Phys.* **1996**, *104*, 7758.
- Jiang, Y.; Zhang, W. Y.; Chen, J. Z. Y. *Phys. Rev. E* **2011**, *84*, 041803.
- Holyst, R.; Oswald, P. *Macromol. Theory Simul.* **2001**, *10*, 1.
- Fredrickson, G. H. *The Equilibrium Theory of Inhomogeneous Polymers*; Clarendon: Oxford, 2006.
- Freed, K. *Adv. Chem. Phys.* **1972**, *22*, 1.
- Liang, Q.; Li, J. F.; Zhang, P. W.; Chen, J. Z. Y. *J. Chem. Phys.* **2013**, *138*, 244910.
- Cui, S. M.; Akcakir, O.; Chen, J. Z. Y. *Phys. Rev. E: Stat. Phys., Plasmas, Fluids, Relat. Interdiscip. Top.* **1995**, *51*, 4548.
- Düchs, D.; Sullivan, D. E. *J. Phys.: Condens. Matter* **2002**, *14*, 12189.

- (39) Song, W.; Tang, P.; Zhang, H.; Yang, Y.; Shi, A. C. *Macromolecules* **2009**, *42*, 6300.
- (40) Shah, M.; Ganesan, V. *J. Chem. Phys.* **2009**, *130*, 054904.
- (41) Deng, M.; Jiang, Y.; Liang, H.; Chen, J. Z. Y. *Macromolecules* **2010**, *43*, 3455.
- (42) Jiang, Y.; Chen, J. Z. Y. *Macromolecules* **2010**, *43*, 10668.
- (43) Kumar, N. A.; Ganesan, V. *J. Chem. Phys.* **2012**, *136*, 101101.
- (44) Song, W. D.; Tang, P.; Qiu, F.; Yang, Y.; Shi, A. C. *Soft Matter* **2011**, *7*, 929.
- (45) Gao, J.; Tang, P.; Yang, Y. L. *Soft Matter* **2011**, *7*, 5208.
- (46) Matsen, M. W. *J. Phys.: Condens. Matter* **2002**, *14*, R21.
- (47) Bates, F. S.; Schulz, M. F.; Khandpur, A. K.; Förster, S.; Rosedale, J. H.; Almdal, K.; Mortensen, K. *Faraday Discuss.* **1994**, *98*, 7.
- (48) Zhang, X.; Jiang, Y.; Miao, B.; Chen, Y.; Yan, D.; Chen, J. Z. Y. *Soft Matter* **2014**, *10*, 5405.
- (49) Zhang, X.; Jiang, Y.; Yan, D.; Chen, J. Z. Y. Manuscript in preparation.
- (50) Perroni, D. V.; Mahanthappa, M. K. *Soft Matter* **2013**, *9*, 7919.
- (51) Goran, U.; Yongsong, L.; Xiangbing, Z.; Virgil, P.; Wook-Dong, C. *Science* **2003**, *299*, 1208.
- (52) Mihai, P.; Virgil, P. *Science* **2010**, *330*, 333.
- (53) Iacovella, C. R.; Keys, A. S.; Glotzer, S. C. *Proc. Natl. Acad. Sci. U. S. A.* **2011**, *108*, 20935.
- (54) Huang, M.; Hsu, C.-H.; Wang, J.; Mei, S.; Dong, X.; Li, Y.; Li, M.; Liu, H.; Zhang, W.; Aida, T.; Zhang, W.-B.; Yue, K.; Cheng, S. Z. D. *Science* **2015**, *348*, 424–428.
- (55) Grason, G. M.; DiDonna, B. A.; Kamien, R. D. *Phys. Rev. Lett.* **2003**, *91*, 058304.
- (56) Grason, G. M.; Kamien, R. D. *Macromolecules* **2004**, *37*, 7371.
- (57) Matsen, M. W. *Macromolecules* **2012**, *45*, 2161.
- (58) Xie, N.; Li, W.; Qiu, F.; Shi, A.-C. *ACS Macro Lett.* **2014**, *3*, 906.
- (59) Thomson, W. *Philos. Mag.* **1887**, *24*, 503.
- (60) Erukhimovich, I.; Kriksin, Y.; ten Brinke, G. *Macromolecules* **2015**, *48*, 7909.
- (61) Erukhimovich, I. Y. *Eur. Phys. J. E: Soft Matter Biol. Phys.* **2005**, *18*, 383.
- (62) Ullal, C. K.; Maldovan, M.; Thomas, E. L.; Chen, G.; Han, Y. J.; Yang, S. *Appl. Phys. Lett.* **2004**, *84*, 5434.
- (63) Maldovan, M.; Thomas, E. L. *Nat. Mater.* **2004**, *3*, 593.
- (64) Hsueh, H. Y.; Chen, H. Y.; She, M. S.; Chen, C. K.; Ho, R. M.; Gwo, S.; Hasegawa, H.; Thomas, E. L. *Nano Lett.* **2010**, *10*, 4994.
- (65) Crossland, E. J. W.; Kamperman, M.; Nedelcu, M.; Ducati, C.; Wiesner, U.; Smilgies, D. M.; Toombes, G. E. S.; Hillmyer, M. A.; Ludwigs, S.; Steiner, U.; Snaith, H. J. *Nano Lett.* **2009**, *9*, 2807.
- (66) Thomas, E. L.; Alward, D. B.; Kinning, D. J.; Martin, D. C.; Handlin, D. L.; Fetter, L. J. *Macromolecules* **1986**, *19*, 2197.
- (67) Matsen, M. W.; Schick, M. *Macromolecules* **1994**, *27*, 4014.
- (68) Vavasour, J. D.; Whitmore, M. D. *Macromolecules* **1993**, *26*, 7070.
- (69) Kriksin, Y. A.; Erukhimovich, I. Y.; Khalatur, P. G.; Smirnova, Y. G.; ten Brinke, G. *J. Chem. Phys.* **2008**, *128*, 244903.
- (70) Kriksin, Y. A.; Khalatur, P. G.; Erukhimovich, I. Y.; ten Brinke, G.; Khokhlov, A. R. *Soft Matter* **2009**, *5*, 2896.
- (71) Matsen, M. W.; Bates, F. S. *Macromolecules* **1996**, *29*, 1091.
- (72) Matsen, M. W.; Bates, F. S. *J. Chem. Phys.* **1997**, *106*, 2436.
- (73) Grason, G. M. *Phys. Rep.* **2006**, *433*, 1.
- (74) Gido, S. P.; Schwark, D. W.; Thomas, E. L.; do Carmo Goncalves, M. *Macromolecules* **1993**, *26*, 2636.
- (75) Helfand, E.; Tagami, Y. *J. Chem. Phys.* **1972**, *56*, 3592.